Nanoscale

ROYAL SOCIETY OF CHEMISTRY

PAPER

View Article Online
View Journal | View Issue

Cite this: *Nanoscale*, 2022, **14**, 15663

Nano-optical imaging of exciton–plasmon polaritons in WSe_2/Au heterostructures†

Raghunandan B. Iyer,[a,b] Yilong Luan,[a,c] Ruth Shinar, *[b] Joseph Shinar*[a,b,c] and Zhe Fei *[a,c]

Received 6th August 2022,
Accepted 8th October 2022

DOI: 10.1039/d2nr04321a

rsc.li/nanoscale

We report a nano-optical imaging study of exciton–plasmon polaritons (EPPs) in WSe_2/Au heterostructures with scattering-type scanning near-field optical microscopy (s-SNOM). By mapping the interference fringes of EPPs at various excitation energies, we constructed the dispersion diagram of the EPPs, which shows strong exciton–plasmon coupling with a sizable Rabi splitting energy (~0.19 eV). Furthermore, we found a sensitive dependence of the polariton wavelength (λ_p) on WSe_2 thickness (d). When d is below 40 nm, λ_p decreases rapidly with increasing d. As d reaches 50 nm and above, λ_p drops to 210 nm, which is over 4 times smaller than that of the free-space photons. Our simulations indicate that the high spatial confinement of EPPs is due to the strong localization of the polariton field inside WSe_2. Our work uncovers the transport properties of EPPs and paves the way for future applications of these highly confined polaritons in nanophotonics and optoelectronics.

Introduction

Exciton–plasmon polaritons (EPP) are hybrid nanophotonic modes formed due to the coupling of surface plasmons polaritons (SPPs) with excitons – bound states of electrons and holes.[1–11] Due to the field localization and enhancement of SPPs, the hybrid EPPs often demonstrate strong plasmon–exciton interactions, which is ideal for many potential applications, including surface-enhanced Raman spectroscopy, solar harvesting, and polariton emission.[11] Common EPP devices are constructed using noble metals interfacing a variety of excitonic materials, including organic molecules and semiconductors. While organic molecules support strongly bounded excitons, they often suffer from fast degradations at elevated temperatures or upon exposure to air and light. Therefore, crystalline semiconductors are often used to enable high device stability under long-term usage. Traditional III–V semiconductors (*e.g.*, GaAs, GaN, *etc.*) with an exciton binding energy of 20–30 meV support exciton polaritons (EPs) and EPPs at cryogenic temperatures.[1,12–15] In recent years, van der Waals (vdW) semiconductors have been widely explored in polaritonic studies due to their strongly-bound excitons.[16–22] The exciton binding energy of these vdW materials is 60–100 meV in the bulk and can reach hundreds of meV when thinning to atomic layers.[23–26] As a result, EPs and EPPs in these layered semiconductors are stable even at room temperature. So far, studies of EPPs in vdW semiconductors were mainly performed with far-field spectroscopy.[5–10] Real-space imaging studies of these hybrid modes have not been reported.

In this work, we performed a comprehensive nano-optical imaging study of EPPs in heterostructures of thin tungsten diselenide (WSe_2) flakes on gold (Au) films. WSe_2 is a group IVB transition metal dichalcogenide (TMD) and a prototypical vdW semiconductor. The two neutral excitons (*i.e.*, A- and B-excitons) of WSe_2 are at around 1.6 eV and 2.1 eV, respectively.[21,27] The WSe_2 thin-flake samples used in our experiments were prepared by mechanical exfoliation of bulk WSe_2 and were then transferred onto a thin Au film on a silicon wafer. For nano-optical imaging, we employed a scattering-type scanning near-field optical microscope (s-SNOM) that was built on an atomic force microscope (AFM). The s-SNOM probes used in our work were metal-coated silicon tips with a radius of curvature of ~25 nm at their apex, which defines the spatial resolution. For EPP excitations (see Fig. 1a), we illuminated the s-SNOM probe with a continuous-wave Ti:sapphire laser. The spectral range of the laser is 1.3–1.8 eV, which covers the A-exciton energy of WSe_2. The laser is set to be in p polarization, which is ideal for the tip enhancement and the excitation of SPPs and EPPs.

---

[a] *Ames Laboratory, U. S. Department of Energy, Iowa State University, Ames, Iowa 50011, USA. E-mail: jshinar@iastate.edu, zfei@iastate.edu*
[b] *Department of Electrical & Computer Engineering, Iowa State University, Ames, Iowa 50011, USA. E-mail: rshinar@iastate.edu*
[c] *Department of Physics and Astronomy, Iowa State University, Ames, Iowa 50011, USA*

† Electronic supplementary information (ESI) available. See DOI: **https://doi.org/10.1039/d2nr04321a**

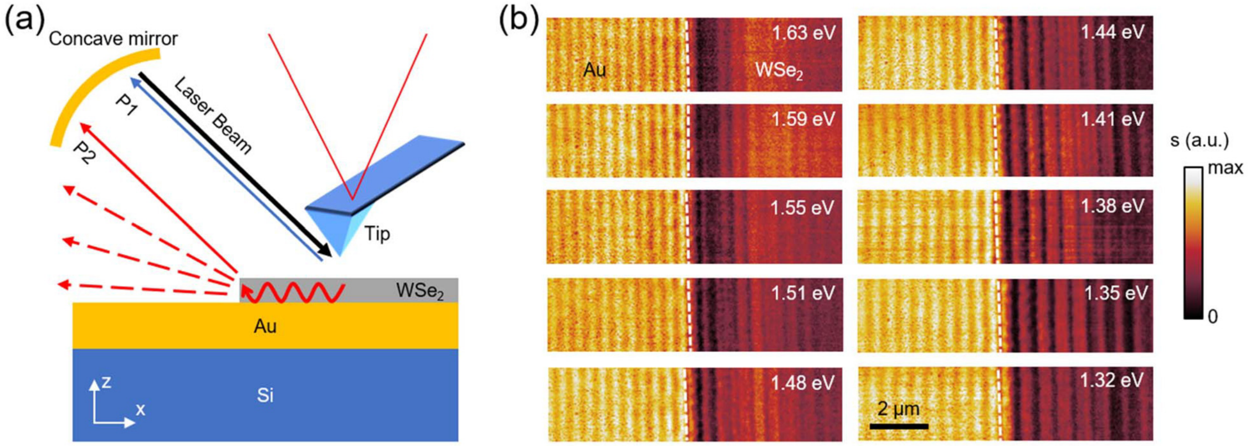

Fig. 1 (a) Illustration of nano-optical imaging experiment of a WSe_2/Au heterostructure sample. (b) The near-field amplitude images of a typical WSe_2/Au heterostructure taken at various excitation energies. The white dashed line marks the edge of the WSe_2 flake.

Results and discussion

Near-field imaging of EPPs

In Fig. 1b, we plot the near-field amplitude images obtained with s-SNOM at various excitation energies (E) on a typical WSe_2/Au heterostructure sample. In this sample, the thickness of WSe_2 (d) is 45 nm, and the thickness of the Au film is 100 nm. As illustrated in Fig. 1a, the WSe_2 flake is on the right half of the images, and the bare Au film is on the left. We used white dashed lines to mark the edge of the WSe_2 flake in Fig. 1b. The laser beam is aligned perpendicular to the WSe_2 edge. From Fig. 1b, one can observe bright fringes on both the Au and WSe_2 sides of the sample. These fringes are parallel to the WSe_2 edge and extend microns away from the edge. By tuning the laser energy, we found that the fringe pattern demonstrates a systematic variation. As introduced in previous studies,[20–22,28–30] such fringes are generated due to the interference between tip-backscattered photons [labeled as "P1" in Fig. 1a] and beam paths involving propagative in-plane modes. A common type of beam path is labeled as "P2" in Fig. 1a,

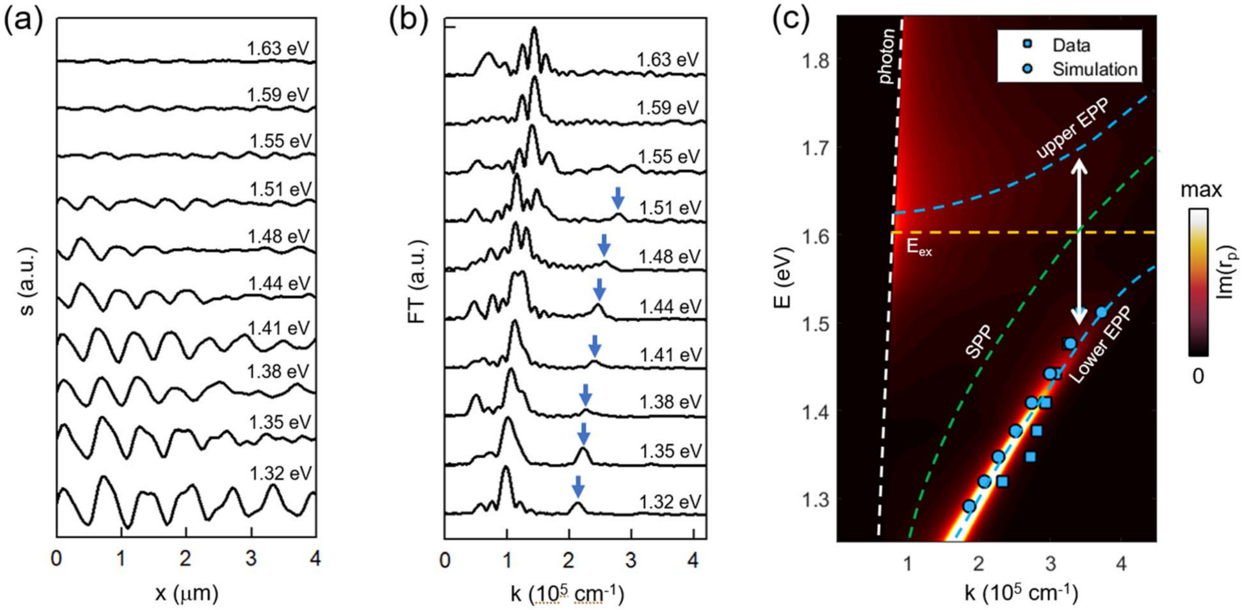

Fig. 2 (a) Energy-dependent fringe profiles (background subtracted) extracted from near-field images in Fig. 1. (b) Fourier-transform (FT) of the fringe profiles in panel (a). The arrows mark the peak associated with EPP interference involving beam paths 'P1' and 'P2'. (c) Dispersion diagrams of EPPs in a 45-nm-thick WSe_2 flake on a thin Au film obtained from theoretical calculations (colormap), experimental data (squares), and finite-element simulations (circles). The colormap plots the imaginary part of the reflection coefficient Im(r_p). The white and orange dashed lines mark the free-space photon and A-exciton energy. The green dashed curves mark the SPP mode without coupling with excitons (see Fig. S5 in ESI†). The blue dashed curves mark the upper and lower branches of the EPP mode.

where tip-excited in-plane modes propagate toward the edge of WSe_2 and then get scattered into photons that are collected by the detector. In the ESI (Fig. S9†), we discuss another possible beam path that is responsible for the generation of the interference fringes. The in-plane modes responsible for the interference fringes on the Au side are SPPs (see Fig. S3 in ESI†). In the main text, we discuss mainly the fringes on the WSe_2 side. Based on the interference mechanism involving beam paths 'P1' and 'P2' (Fig. 1a), we can establish a direct relationship between the fringe period (ρ) and the wavelength of the in-plane mode (λ_p):[20–22]

$$1/\rho = 1/\lambda_p - \cos\alpha/\lambda_0, \tag{1}$$

where λ_0 is the free-space photon wavelength and α is the incident angle of the laser beam ($\alpha \approx 30°$) [see Fig. 1a].

Dispersion analysis of EPPs

To obtain ρ and hence λ_p, we extracted the line profiles perpendicular to the fringes on WSe_2 from Fig. 1b, which are plotted in Fig. 2a. We then performed a Fourier transform (FT) of these profiles to determine ρ. The corresponding FT profiles are plotted in Fig. 2b, where the peaks correspond to $2\pi/\rho$. Here, we noticed two peaks in the FT profiles. The one at a relatively high wavenumber (k) corresponds to interference fringes of EPPs generated by beam paths 'P1' and 'P2'. The lower-k peak, which sits roughly at half the k coordinates, is generated due to a more complicated interference process involving additional beam paths (see detailed discussions in the ESI†). With Fourier analysis and eqn (1), we were able to determine λ_p and mode wavevector ($k_p = 2\pi/\lambda_p$) at various excitation energies, based on which we constructed the $E - k_p$ dispersion relationship of the in-plane mode. The experimental dispersion is shown in Fig. 2c as squares. Besides, we also plot the dispersion relation obtained from finite-element simulations (circles) (see Fig. S4 in ESI†). Both data points are sitting on a theoretical dispersion colormap, where we plot the imaginary part of the p-polarized reflection coefficient (r_p). The bright curves revealed by the colormap correspond to the photonic or polaritonic modes in the system. Here we can see a high-wavevector mode on the right side of the photon line, which matches well the experimental and simulation data points.

The bright mode marked with blue dashed curves in Fig. 2c corresponds to the EPP mode, which is generated due to the coupling between the SPP mode of Au and the A exciton of WSe_2. Due to the coupling, the bare plasmonic mode is split into two polaritonic branches (upper and lower branches). The Rabi splitting energy Ω_R of the two branches is estimated to be 0.19 eV (marked with arrow), higher than the average linewidth of exciton and plasmon modes $(\gamma_{ex} + \gamma_p)/2 \approx 0.09$ eV (see

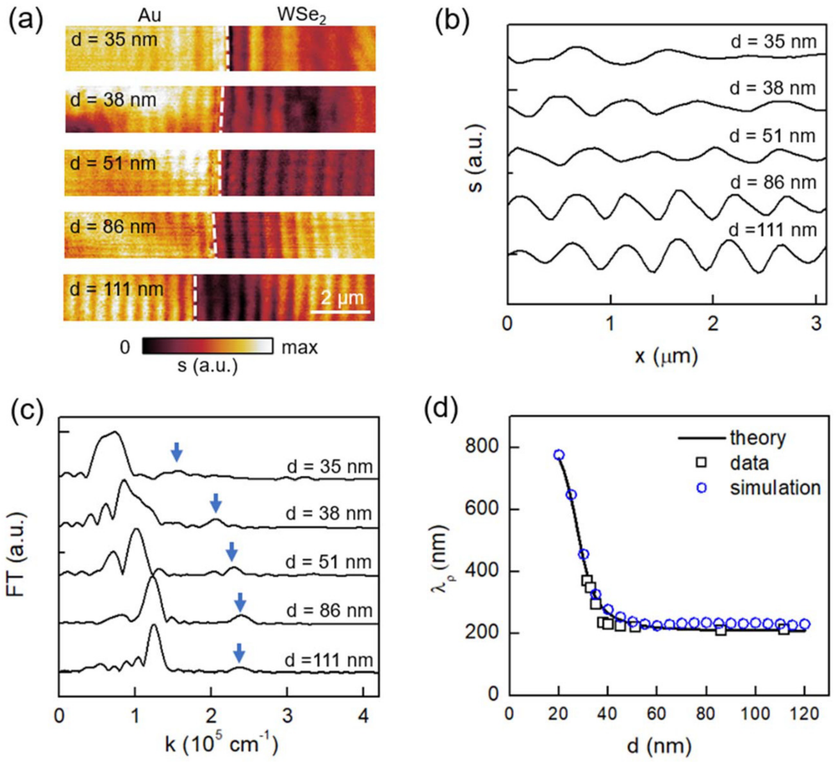

Fig. 3 (a) The near-field amplitude images of WSe_2/Au heterostructure waveguides with various WSe_2 thicknesses (d). The excitation energy was set to be E = 1.38 eV. (b) The fringe profiles (background subtracted) extracted from near-field images in panel (a). (c) Fourier-transform of the fringe profiles in panel (b). The arrows mark the peak associated with EPP interference involving beam paths 'P1' and 'P2'. (d) The EPP wavelengths as a function of WSe_2 thickness from theoretical calculations (curve), experimental data (squares), and finite-element simulations (circles).

section 4 in ESI†). Therefore, the measured EPP mode is in the strong coupling regime. As discussed in the ESI,† the Rabi splitting energy and the exciton–plasmon coupling are sensitively dependent on the thickness of WSe_2. Note that the upper branch of the EPP mode is relatively flat (*i.e.*, less propagative) and strongly damped, so it is not measurable by near-field imaging. In our s-SNOM imaging experiment, we focus mainly on the lower branch of the EPP mode, which is highly dispersive with small damping.

Thickness dependence of EPPs

Finally, we wish to explore the dependence of the EPP mode on the thickness of the WSe_2 flake (d). In Fig. 3a, we plot the near-field amplitude images taken at E = 1.38 eV from WSe_2/Au heterostructures with various WSe_2 thicknesses. We found that the bright fringes are sensitively dependent on d. We then extracted the line profiles across the fringes and performed Fourier analysis. In Fig. 3b and c, we plot the fringe profiles and the corresponding FT profiles respectively, based on which we obtained the EPP wavelength with eqn (1). The d-dependent λ_p from the fringe analysis is plotted in Fig. 3d, which agrees with the theoretical calculations and finite-element simulations (see discussions below). From Fig. 3d, we found that λ_p decreases rapidly with increasing WSe_2 thicknesses for $d \leq 40$ nm. As d increases to 50 nm and above, λ_p approaches ~210 nm, which is less than a quarter of the free-space photon wavelength. Such high spatial confinement is rarely seen in other polaritonic or plasmonic modes in the near-IR frequency range. The EPP wavelength becomes less sensitive on d for WSe_2 flakes thicker than 50 nm.

To understand the thickness dependence of λ_p (Fig. 3d), we performed finite-element simulations of the EPP mode at E = 1.38 eV with COMSOL Multiphysics. As sketched in Fig. 4a, we constructed the air/WSe_2/Au/Si four-layer heterostructure model. The EPPs are launched from left to right along the x axis (marked with an arrow in Fig. 4a). In Fig. 4b, we plot the simulated E_z field maps of the EPP mode for WSe_2 with different thicknesses. When the thickness of WSe_2 is very small (*e.g.*, $d \leq 20$ nm), the polariton field is mainly inside the air. As d increases, the polariton field is confined more and more inside WSe_2 resulting in strong light–matter interactions. As a result, λ_p decreases systematically with increasing WSe_2 thickness. For $d \geq 50$ nm, the polariton field is localized completely inside WSe_2, thus enabling the highest spatial confine-

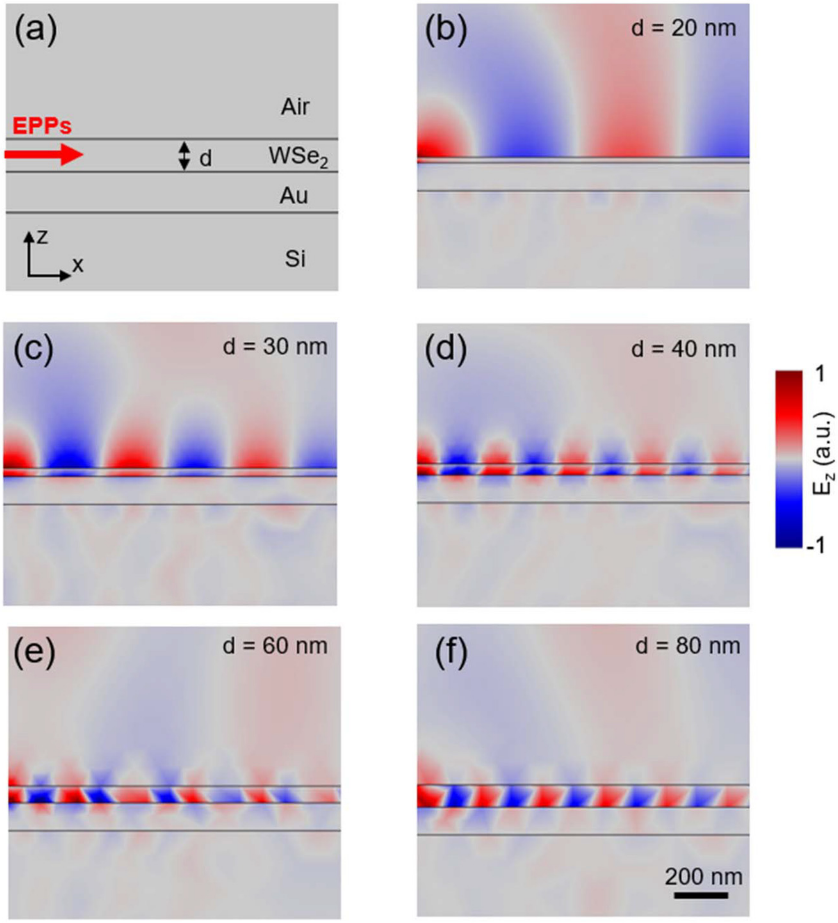

Fig. 4 (a) Sketch of the air/WSe_2/Au/SiO_2 four-layer heterostructure model for EPP simulations. (b)–(f) The simulated E_z field maps of the EPP mode inside the WSe_2/Au heterostructure with various WSe_2 thicknesses. The excitation energy is E = 1.38 eV.

ment. Further increase of the WSe_2 thickness does not significantly affect the field distribution and hence the polariton wavelength.

Conclusions

In summary, we have performed a comprehensive nano-optical study of the hybrid EPP modes at the WSe_2/Au interface, which were formed due to the strong coupling between SPPs on gold and excitons in WSe_2. By imaging and analyzing the interference patterns of the EPPs, we were able to determine their wavelengths and construct the dispersion diagram. In addition, we found the EPP wavelength decreases systematically as WSe_2 thickness increases, which is due to the stronger localization of the polariton field inside WSe_2. The ultimate polariton confinement can be achieved as WSe_2 thickness reaches 50 nm and above, where the EPP wavelength is as low as ~210 nm. Compared to waveguide EPs,[20–22] the EPP mode imaged here at the TMD/metal interface is significantly higher confined in space with stronger field enhancement. Both merits are important in technological applications such as on-chip nanophotonic signal processing[31] and bio-sensing,[32] where devices with small footprints and high sensitivity are desirable.

Conflicts of interest

There are no conflicts to declare.

Acknowledgements

This work was supported by the U.S. Department of Energy (DOE), Office of Science, Basic Energy Sciences, Materials Science and Engineering Division. The research was performed at Ames Laboratory, which is operated for the U.S. DOE by Iowa State University under contract # DE-AC02-07CH11358.

References

1 J. Bellessa, C. Symonds, C. Meynaud, J. C. Plenet, E. Cambril, A. Miard, L. Ferlazzo and A. Lemaître, *Phys. Rev. B: Condens. Matter Mater. Phys.*, 2008, **78**, 205326.

2 M. Rödel, P. Lisinetskaya, M. Rudloff, T. Startk, J. Manara, R. Mitric and J. Pflaum, *J. Phys. Chem. C*, 2022, **126**, 4163–4171.

3 P. Törmä and W. L. Barnes, *Rep. Prog. Phys.*, 2015, **78**, 013901.

4 A. Berrier, R. Cools, C. Arnold, P. Offermans, M. Crego-Calama, S. H. Brongersma and J. Gómez-Rivas, *ACS Nano*, 2011, **5**, 6226–6232.

5 N. Lundt, S. Klembt, E. Cherotchenko, S. Betzold, O. Iff, A. V. Nalitov, M. Klaas, C. P. Dietrich, A. V. Kavokin, S. Höfling and C. Schneider, *Nat. Commun.*, 2016, **7**, 13328.

6 B. Lee, W. Liu, C. H. Naylor, J. Park, S. C. Malek, J. S. Berger, A. T. C. Johnson and R. Agarwal, *Nano Lett.*, 2017, **17**, 4541–4547.

7 P. Vasa, R. Pomraenke, S. Schwieger, Y. I. Mazur, V. Kunets, P. Srinivasan, E. Johnson, J. E. Kihm, D. S. Kim, E. Runge, G. Salamo and C. Lienau, *Phys. Rev. Lett.*, 2008, **101**, 116801.

8 P. Ni, A. D. L. Bugallo, V. M. A. Arreola, M. F. Salazar, E. Strupiechonski, V. Brandli, R. Sawant, B. Alloing and P. Genevet, *ACS Photonics*, 2019, **6**, 1594–1601.

9 R. K. Chowdhury, P. K. Datta, S. N. B. Bhaktha and S. K. Ray, *Adv. Opt. Mater.*, 2020, **8**, 1901645.

10 H. Zhang, B. Abhiraman, Q. Zhang, J. Miao, K. Jo, S. Roccasecca, M. W. Knight, A. R. Davoyan and D. Jariwala, *Nat. Commun.*, 2020, **11**, 3552.

11 E. Cao, W. Lin, M. Sun, W. Liang and Y. Song, *Nanophotonics*, 2018, **7**, 145–167.

12 C. Weisbuch, M. Nishioka, A. Ishikawa and Y. Arakawa, *Phys. Rev. Lett.*, 1992, **69**, 3314–3317.

13 H. M. Gibbs, G. Khitrova and S. W. Koch, *Nat. Photonics*, 2011, **5**, 273.

14 F. Tassone, F. Bassani and L. C. Andreani, *Phys. Rev. B: Condens. Matter Mater. Phys.*, 1992, **45**, 6023–6030.

15 H. Deng, H. Haug and Y. Yamamoto, *Rev. Mod. Phys.*, 2010, **82**, 1489–1537.

16 D. N. Basov, M. M. Fogler and F. J. García de Abajo, *Science*, 2016, **354**, 6309.

17 T. Low, A. Chaves, J. D. Caldwell, A. Kumar, N. X. Fang, P. Avouris, T. F. Heinz, F. Guinea, L. Martin-Moreno and F. Koppens, *Nat. Mater.*, 2017, **16**, 182–184.

18 X. Liu, T. Galfsky, Z. Sun, F. Xia, E.-C. Lin, Y.-H. Lee, S. Kéna-Cohen and V. M. Menon, *Nat. Photonics*, 2015, **9**, 30–34.

19 S. Dufferwiel, S. Schwarz, F. Withers, A. A. P. Trichet, F. Li, M. Sich, O. Del Pozo-Zamudio, C. Clark, A. Nalitov, D. D. Solnyshkov, G. Malpuech, K. S. Novoselov, J. M. Smith, M. S. Skolnick, D. N. Krizhanovskii and A. I. Tartakovskii, *Nat. Commun.*, 2015, **6**, 8579.

20 F. Hu, Y. Luan, M. E. Scott, J. Yan, D. G. Mandrus, X. Xu and Z. Fei, *Nat. Photonics*, 2017, **11**, 356–360.

21 F. Hu, Y. Luan, J. Speltz, D. Zhong, C. H. Liu, J. Yan, D. G. Mandrus, X. Xu and Z. Fei, *Phys. Rev. B*, 2019, **100**, 121301(R).

22 Y. Luan, H. Zobeiri, X. Wang, E. Sutter, P. Sutter and Z. Fei, *Nano Lett.*, 2022, **22**, 1497–1503.

23 N. Saigal, V. Sugunakar and S. Ghosh, Exciton binding energy in bulk MoS_2: A reassessment, *Appl. Phys. Lett.*, 2016, **108**, 132105.

24 A. Chernikov, T. C. Berkelbach, H. M. Hill, A. Rigosi, Y. Li, O. B. Aslan, D. R. Reichman, M. S. Hybertsen and T. F. Heinz, *Phys. Rev. Lett.*, 2014, **113**, 076802.

25 K. He, N. Kumar, L. Zhao, Z. Wang, K. F. Mak, H. Zhao and J. Shan, *Phys. Rev. Lett.*, 2014, **113**, 026803.

26 A. T. Hanbicki, M. Currie, G. Kioseoglou, A. L. Friedman and B. T. Jonker, *Solid State Commun.*, 2015, **203**, 16–20.

27 A. R. Beal, W. Y. Liang and H. P. Hughes, *J. Phys. C: Solid State Phys.*, 1976, **9**, 2449–2457.

28 M. Mrejen, L. Yadgarov, A. Levanon and H. Suchowski, *Sci. Adv.*, 2019, **5**, eaat9618.

29 D. Hu, X. Yang, C. Li, R. Liu, Z. Yao, H. Hu, S. N. G. Corder, J. Chen, Z. Sun, M. Liu and Q. Dai, *Nat. Commun.*, 2017, **8**, 1471.

30 A. J. Sternbach, S. Latini, S. Chae, H. Hübener, U. D. Giovannini, Y. Shao, L. Xiong, Z. Sun, N. Shi, P. Kissin, G.-X. Ni, D. Rhodes, B. Kim, N. Yu, A. J. Millis, M. M. Fogler, P. J. Schuck, M. Lipson, X.-Y. Zhu, J. Hone, R. D. Averitt, A. Rubio and D. N. Basov, *Nat. Commun.*, 2020, **11**, 3567.

31 Y. Fang and M. Sun, *Light: Sci. Appl.*, 2015, **4**, e294.

32 S.-H. Oh, H. Altug, X. Jin, T. Low, S. J. Koester, A. P. Ivanov, J. B. Edel, P. Avouris and M. S. Strano, *Nat. Commun.*, 2021, **12**, 3824.